

## Phase stability and micromechanical properties of TiZrHf-based refractory high-entropy alloys: A first-principles study

Xiaoqing Li\*

*Applied Materials Physics, Department of Materials Science and Engineering, KTH-Royal Institute of Technology, Stockholm SE-10044, Sweden*



(Received 28 July 2023; accepted 19 October 2023; published 13 November 2023)

Endowing room-temperature ductility in refractory high-entropy alloys (RHEAs) is a challenge to their uses in nuclear energy systems, biomedical, and high-temperature applications. Recently, transformation-induced plasticity (TRIP) has been recognized as an effective strategy to simultaneously improve ductility and tensile strength of RHEAs. Hitherto, the design for a TRIP mechanism in RHEAs through material-dependent parameters typically follows empirical approaches. Here, we investigate the alloying effect of several body-centered cubic (bcc) transition metal elements (TM=V, Nb, Cr, Mo, and W) on the phase stability and the micromechanical properties of the TiZrHf alloy using a first-principles method. We show that the addition of the considered TM elements increases the stability of the bcc phase relative to the hexagonal close-packed (hcp) phase and the relative stability between these two phases can be tuned and inverted. We investigate the composition-dependent single-crystal elastic constants for the  $(\text{TiZrHf})_{1-x}\text{Nb}_x$  and  $(\text{TiZrHf})_{1-x}\text{Mo}_x$  alloys and analyze mechanical stability, elastic anisotropy, and polycrystalline moduli. Our results show that the anisotropy of Young's modulus is more pronounced the closer the alloy composition is to the composition where the bcc phase or hcp phase becomes mechanically unstable. We find that the hcp phase has higher shear and Young's moduli than the bcc phase below a critical composition for the Nb or Mo addition, while the bcc phase has larger moduli above the critical composition. Furthermore, our results imply that the  $d$ -band filling has a dominant influence on the phase stability and mechanical properties of the alloys.

DOI: [10.1103/PhysRevMaterials.7.113604](https://doi.org/10.1103/PhysRevMaterials.7.113604)

### I. INTRODUCTION

Since the high-entropy alloy (HEA) concept was reported, it has attracted great attention in the scientific community. Refractory HEAs (RHEAs) are largely or entirely composed of refractory elements, e.g., Zr, Ti, Nb, Cr, and W, and often form a solid solution with single body-centered cubic (bcc) structure. Some RHEAs have excellent high-temperature strength and high melting point [1–4], which render RHEAs interesting for high-temperature applications. For example, the yield stress values of the NbMoTaW and VNbMoTaW RHEAs are much higher than those of Inconel 718 at temperatures above 1073 K, and the yield stress decreased from 561 to 405 MPa and from 862 to 477 MPa for NbMoTaW and VNbMoTaW in the temperature range from 873 to 1873 K, respectively. It was recently suggested [5] that trapping of edge dislocations in the random atomic environments of RHEAs plays an important role in determining the retained strength at high temperature. Some RHEAs, such as ZrNbHf, are considered as a

candidate structure material for nuclear energy systems [6–8] due to their high resistance to irradiation damage. Moreover, the potential of RHEAs as novel implant material has been recognized recently [9–11], e.g., some RHEAs have superior biocompatibility and strength compared to materials currently used.

Lack of room-temperature ductility in most of the RHEAs produced so far is a critical issue, limiting their formability. Several theoretical and experimental lines of study were devoted to endow bcc RHEAs with enhanced ductility [12–19]. Based on the postulate that intrinsic ductility of a material is controlled by its intrinsic fracture behavior at an atomically sharp crack tip [12], theoretical investigations focused on identifying alloy compositions that exhibit an intrinsic resistance to brittle failure [13,14]. An experimental direction of approach, aimed at delaying plastic strain localization, proposed to manage dislocation movement and interactions via incorporating dispersed, nanoscale chemical inhomogeneities, such as precipitate precursors in oxygen-doped TiZrNbHf [15] and incipient spinodal decomposition in TiVNbHf [16]. The benefit of deformation-induced phase transformations [transformation-induced plasticity (TRIP)] to enhance strain hardening capability in regions of strain localization was successfully demonstrated in a proof of concept for several TiZrHf-based RHEAs in bcc structure [17–19]. Instead of seeking to stabilize a single phase as in typical HEA design processes, the basic concept of TRIP RHEAs is to reduce the stability of the bcc phase by varying the

\*xiaoqli@kth.se

*Published by the American Physical Society under the terms of the Creative Commons Attribution 4.0 International license. Further distribution of this work must maintain attribution to the author(s) and the published article's title, journal citation, and DOI. Funded by Bibsam.*

composition until it becomes metastable at room temperature without transforming spontaneously. The energy provided under mechanical loading may drive a martensitic phase transformation from the bcc phase into a compositionally equivalent daughter phase, e.g., a hexagonal close-packed (hcp) phase. For example, two TRIP alloys were developed in the bcc TiZrHfTa<sub>x</sub> alloy system [18] by tuning the composition  $x$ . Strain hardening capability, fracture toughness, and ductility were significantly increased by altering the chemistry to destabilize the bcc structure, and the ultimate tensile strength exceeded 1 GPa in TiZrHfTa<sub>0.4</sub>.

Identifying suitable RHEA compositions in the associated immense composition space that show the TRIP effect requires large experimental efforts. Moreover, the mechanical properties of individual phases, e.g., their elastic moduli and composition dependencies, are highly demanded to achieve desired final properties but may be challenging to measure if the phases are not in equilibrium or dispersed in the alloys. Calculations are an approach to rapidly screen intrinsic properties of materials and to identify promising target alloys. Density-functional theory (DFT) has become a widely recognized tool in materials science to investigate properties of materials. In particular, DFT has demonstrated to provide successful guidance in developing TRIP HEAs [19–21] and predict accurate values for elastic properties of HEAs [22,23].

In this work, we investigate the phase stability and micromechanical properties of (TiZrHf)<sub>1-x</sub>TM<sub>x</sub> (substitution TM=V, Nb, Cr, Mo, and W) alloys with composition  $x$  from 0 to 55 at.% using a first principles method. On the one hand, the results predicted here are expected to aid the development of new high-performance TiZrHf-based TRIP alloys. On the other hand, for some of the previously reported brittle bcc RHEAs, this study would shed new light for manipulating their phase stability by tuning composition to achieve ductile behavior.

## II. METHOD

We employed the exact muffin-tin orbitals (EMTO) method [24,25] to solve the Kohn-Sham equations in DFT [26]. The local-density-approximation functional [27] was adopted to describe exchange and correlation. The total energy was calculated by the full charge-density technique, and the problem of chemical disorder was treated within the coherent-potential approximation (CPA) [28,29]. The Greens function was calculated for 16 complex energy points at the valence states below the Fermi level. We tested convergence carefully with respect to  $k$  points, and we used between  $20 \times 10^3$  and  $25 \times 10^3$  uniformly distributed  $k$  points for the calculations of total energy and elastic constants. For the bcc phase, total energies calculated for seven different atomic volumes were used to obtain the equilibrium volume by fitting a Morse-type function to the calculated energy-volume data. For the hcp phase, we calculated total energies on a grid of eight different atomic volumes and seven hexagonal axial  $c/a$  ratios, and then found the ground state by interpolation as described in Ref. [29]. We employed the same approach to compute the single-crystal elastic constants  $C_{ij}$  as in previous work [29,30].

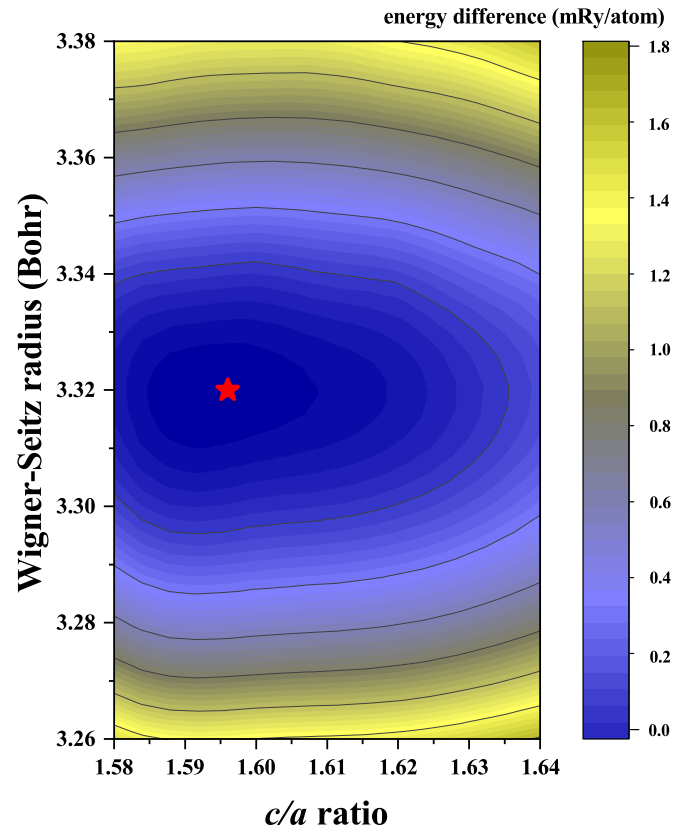


FIG. 1. The total energy difference of the hcp TiZrHf alloy as a function of the Wigner-Seitz radius  $w$  and hexagonal axial ratio  $c/a$ . The energy is relative to the equilibrium marked by the red star.

## III. RESULTS AND DISCUSSION

### A. Equilibrium lattice parameters

In Fig. 1, we show a contour plot of the calculated total energies of the hcp TiZrHf alloy as a function of the Wigner-Seitz radius  $w$  and the  $c/a$  ratio. An equilibrium configuration with  $w$  and  $c/a$  values about 3.32 Bohr and 1.596 was determined, respectively. Comparing to the recent experimental data ( $w=3.254(4)$  Bohr [31], 3.204 Bohr [32], and  $c/a=1.582(2)$  [31], 1.586 [32]), our theoretical values deviate by about 2–4% for  $w$  and below 1% for  $c/a$ . Figures 2(a)–2(c) show the calculated  $w$  and  $c/a$  ratios for (TiZrHf)<sub>1-x</sub>TM<sub>x</sub> (TM=V, Nb, Cr, Mo, and W) alloys in their bcc and hcp phases. One can see that the addition of any of the TM elements leads to a volumetric contraction with  $x$  in both the bcc and hcp phases. The volumetric contractions are the strongest with adding Cr and the weakest with Nb, and Mo and W have similar, intermediate effects on the  $w$ . In Fig. 2(c) an expansion of the  $c/a$  ratio with  $x$  in all the alloys is observed. The relative increase of  $c/a$  is the largest for W and the smallest for V.

### B. Phase stability

A fast and useful guidance to predict potential alloys with TRIP behavior is to assess the chemical driving force for the martensitic transition, which is governed by the Gibbs energy difference of parent and daughter phases [33,34].

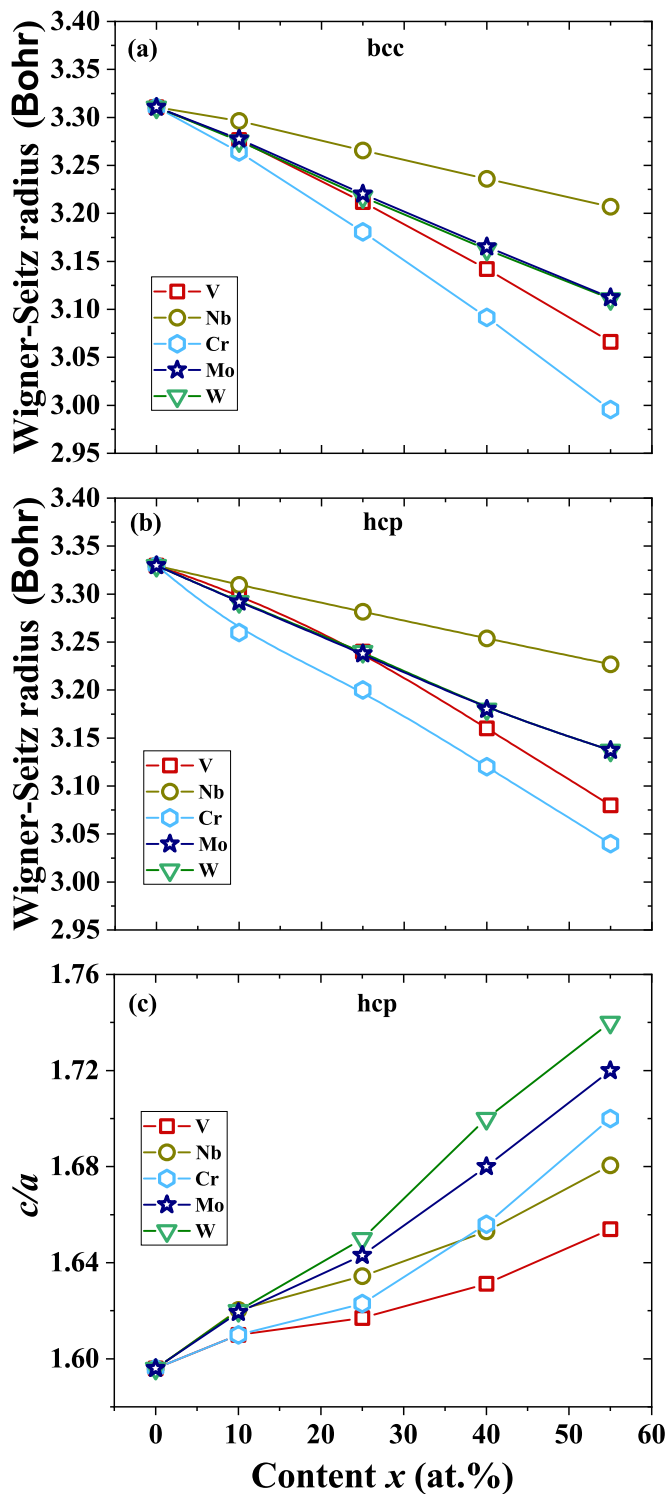


FIG. 2. The Wigner-Seitz radius  $w$  of  $(\text{TiZrHf})_{1-x}\text{TM}_x$  alloys in the bcc and hcp phases and the hexagonal axial ratio  $c/a$  in the hcp phase.

Focusing on the athermal limit, we investigate the total energy difference of the bcc phase against the hcp phase for the  $(\text{TiZrHf})_{1-x}\text{TM}_x$  (TM=V, Nb, Cr, Mo, and W) alloys, i.e.,  $\Delta E^{\text{bcc-hcp}} = E^{\text{bcc}} - E^{\text{hcp}}$  as a function of concentration  $x$ . In Fig. 3,  $\Delta E^{\text{bcc-hcp}}$  of TiZrHf alloy is positive, indicating that the hcp phase is more stable than the bcc phase, in agreement

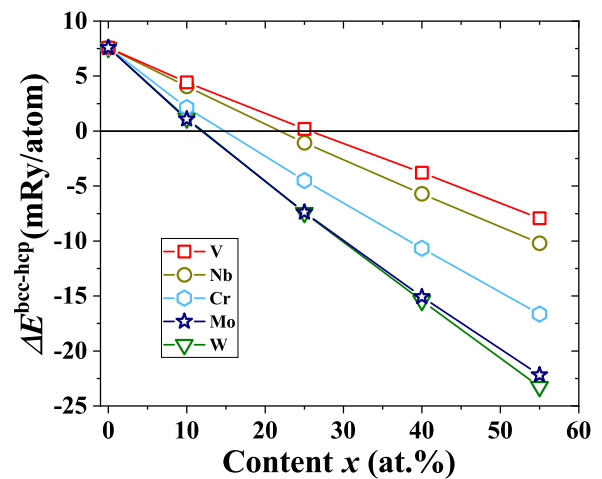


FIG. 3. The total energy difference of the bcc phase relative to the hcp phase for the  $(\text{TiZrHf})_{1-x}\text{TM}_x$  (TM=V, Nb, Cr, Mo, and W) alloys.

with the experimental result that hcp TiZrHf phase is stable at ambient temperature and pressure [31,35]. With introducing any of the TM elements,  $\Delta E^{\text{bcc-hcp}}$  decreases with increasing  $x$  and turns negative at a critical concentration. The calculated critical concentrations are about 25 at.%, 22 at.%, 15 at.%, and 12 at.% for addition of V, Nb, Cr, and W/Mo, respectively. The elements Cr, Mo, and W are stronger bcc stabilizers than Nb and V based on how much  $\Delta E^{\text{bcc-hcp}}$  changes with  $x$ . These results indicate that the relative stability between compositionally identical bcc and hcp phases can be tuned and inverted. Relative to Cr, Mo, or W, addition of V or Nb offers a larger composition interval where the bcc phase is metastable and may transform to the hcp phase by mechanical loading.

### C. Electronic structure

The volumetric contractions of the Wigner-Seitz radius and expansions of the hcp  $c/a$  ratio (Fig. 2) and the relative stabilization of the bcc phase (lowering of  $\Delta E^{\text{bcc-hcp}}$ , Fig. 3) increase with the addition of TM that have more filled  $d$  bands than Ti, Zr, and Hf (electronic configuration  $d^2s^2$ ). Cr, Mo, and W with two additional electrons ( $d^4s^2$ ) have larger alloying effects than V and Nb ( $d^3s^2$ ) due to their relatively larger filling of the  $d$  band. The calculated trends are congruent with the canonical band picture of the transition metal series [36–38], which predicts structure parameters and structural energy differences of unaries as a function of the electronic  $d$ -band filling. The canonical picture is expected to describe transition metal alloys: which constituent elements have similar electronic configuration more closely than alloys which constituent elements vary starkly in electronic configuration.

To obtain a rough understanding of the electronic structure of TiZrHf and the effect of alloying, below we look into the electronic density of states (DOS). We focus on the bcc phase and the quaternaries with 10 at.% Nb and Mo. Choosing two substitutions from the same transition metal series simplifies the discussion of band-filling effects on the DOSs compared to substitutions from different series, where disorder effects

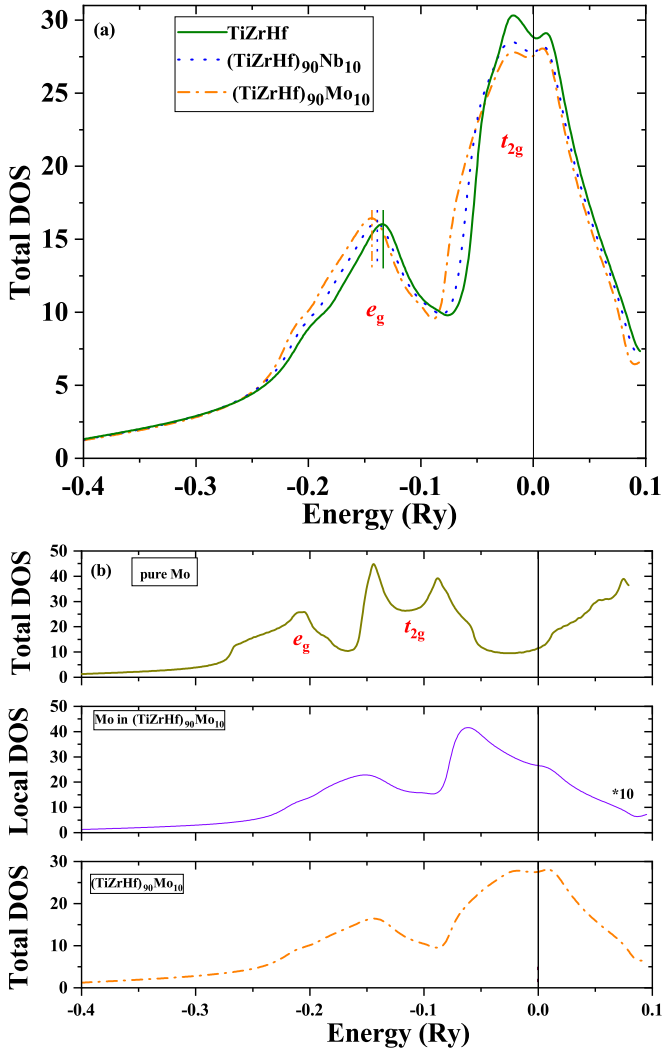


FIG. 4. (a) The total DOS (in units of  $1/\text{Ry}$ ) of TiZrHf,  $(\text{TiZrHf})_{90}\text{Nb}_{10}$ , and  $(\text{TiZrHf})_{90}\text{Mo}_{10}$  alloys in the bcc phase. (b) The total DOS of pure bcc Mo calculated at the equilibrium volume of  $(\text{TiZrHf})_{90}\text{Mo}_{10}$ , the local DOS of Mo in  $(\text{TiZrHf})_{90}\text{Mo}_{10}$  normalized to 100 %, and the total DOS of  $(\text{TiZrHf})_{90}\text{Mo}_{10}$  alloy.

due to different band width are more pronounced. The total DOS of TiZrHf alloy in the bcc phase presented in Fig. 4(a) is governed by an  $spd$  valence band and features two dominant peaks associated with the  $d$  states, a first peak at lower eigenenergies arising from mainly the  $e_g$  states, and a second peak at higher eigenenergies from states with predominantly  $t_{2g}$  character. The position of the Fermi level is placed near the top of the  $t_{2g}$  peak and lies approximately 0.1 Ry below the bcc pseudogap, which roughly separates  $d$  bonding states from antibonding states. Comparison with the DOS of bcc Mo shown in Fig. 4(b) suggests that the typical characteristics of a bcc transition metal DOS are preserved in TiZrHf while also showing disorder induced smearing. Alloying with Nb or Mo broadens the  $e_g$  peak and shifts it to lower eigenenergies, see the vertical lines indicating  $e_g$  peak positions in Fig. 4(a). Alloying also shifts spectral weight from the top of the  $t_{2g}$  peak to its lower energy flank. All in all this suggests an increase of the cohesive energy due to alloying with Nb or Mo.

We further interpret the total alloy DOS in terms of common-band and split-band models [39,40]. In pure metal form, the  $d$ -electron DOSs of Ti, Zr, and Hf are centered at similar energies  $\epsilon$  due to similar electronic configurations.  $\epsilon$  is related to atomiclike  $d$  energy levels. The  $d$  bandwidths of Ti, Zr, and Hf are different and follow a well-known macrotrend,  $\omega_{\text{Ti}} < \omega_{\text{Zr}} < \omega_{\text{Hf}}$  [41]. Upon Ti, Zr, and Hf forming a solid solution, we assume charge neutrality and imagine aligning the Fermi energies. As the energy separation of the  $d$ -band centers of Ti, Zr, and Hf is much smaller than their bandwidths ( $\Delta\epsilon/\omega \ll 1$ ), one expects a common band like alloy DOS with significant hybridization between states associated with the Ti, Zr, and Hf atoms [Fig. 4(a)]. The alloy's  $d$  bandwidth adjusts toward the average over the constituent elements to maximize hybridization.

The  $d$ -electron centers of Nb and Mo are lower in energy relative to the TiZrHf ternary in accordance with their higher  $d$ -occupation numbers. In bcc Mo, the Fermi level is placed near the top of the pseudogap, see Fig. 4(b), and in bcc Nb near the bottom of the pseudogap (not shown). Within a  $d$ -block series, there is a microtrend in the  $d$  bandwidths, i.e.,  $\omega_{\text{Zr}} > \omega_{\text{Nb}} > \omega_{\text{Mo}}$  [41], but this variation is less pronounced than the macrotrend across the  $3d$ ,  $4d$ , and  $5d$  blocks. As before in TiZrHf we assume charge neutrality and imagine aligning the Fermi levels. The energy separation between the  $d$ -band centers of Mo and TiZrHf is still smaller than their  $d$  bandwidths, suggesting mainly a common-band type behavior in  $(\text{TiZrHf})_{1-x}\text{Mo}_x$ , but more pronounced alloy disorder effects are expected. This is illustrated in Fig. 4(b) for the DOS associated with Mo atoms in  $(\text{TiZrHf})_{90}\text{Mo}_{10}$ . Disorder effects on Mo are most significant for the  $t_{2g}$  peak. There is also a shift of the electronic states to higher eigenenergies, apparent from the positions of the band bottom and  $e_g$  and  $t_{2g}$  peaks, which benefits hybridization with the TiZrHf states. This upshift of the valence band is, in parts, compensated by spectral weight redistribution within the  $t_{2g}$  peak toward lower energies. Effectively, there is a slight charge transfer from Mo to the host states. Similar but less pronounced effects occur upon alloying TiZrHf with Nb.

#### D. Mechanical stability

The elastic properties of a single-crystal solid can be described by the elastic constants  $C_{ij}$ . Cubic structures have three independent single-crystal elastic constants, i.e.,  $C_{11}^{\text{bcc}}$ ,  $C_{12}^{\text{bcc}}$ , and  $C_{44}^{\text{bcc}}$ , whereas there are five independent single-crystal elastic constants for hexagonal structures, namely  $C_{11}^{\text{hcp}}$ ,  $C_{12}^{\text{hcp}}$ ,  $C_{13}^{\text{hcp}}$ ,  $C_{33}^{\text{hcp}}$ , and  $C_{44}^{\text{hcp}}$ .

Here, we choose and compare the weak bcc stabilizer Nb and the strong bcc stabilizer Mo as two representative substitutions and calculate the composition-dependent single-crystal elastic constants of  $(\text{TiZrHf})_{1-x}\text{Nb}_x$  and  $(\text{TiZrHf})_{1-x}\text{Mo}_x$  in both the bcc and hcp phases. Figures 5(a) and 5(b) present the  $C_{ij}$  in the bcc phase. We can see that the addition of Nb or Mo hardens  $C_{11}^{\text{bcc}}$  and softens  $C_{44}^{\text{bcc}}$ , while alloying has a weak effect on  $C_{12}^{\text{bcc}}$ . Comparing with the Nb addition, the addition of Mo has a stronger effect on the  $C_{ij}$ . The composition dependence of  $C_{ij}$  in the hcp phase is displayed in Figs. 5(c) and 5(d). The values of both

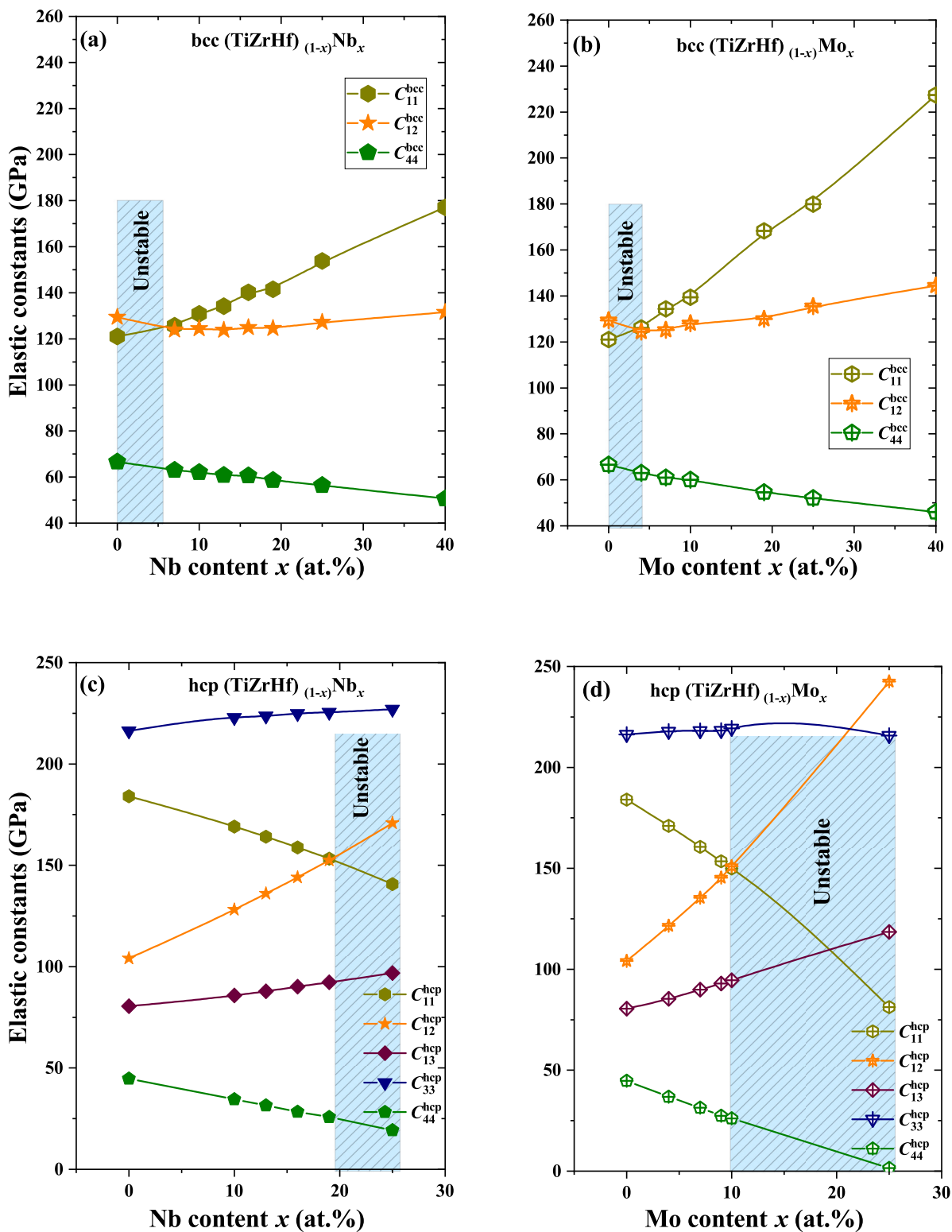


FIG. 5. The calculated composition dependence of single-crystal elastic constants for the  $(\text{TiZrHf})_{1-x}\text{Nb}_x$  and  $(\text{TiZrHf})_{1-x}\text{Mo}_x$  alloys in their bcc and hcp phases. Composition intervals where the alloys are mechanically unstable are highlighted.

$C_{12}^{\text{hcp}}$  and  $C_{13}^{\text{hcp}}$  increase with increasing the content of Nb or Mo, whereas  $C_{11}^{\text{hcp}}$  and  $C_{44}^{\text{hcp}}$  decrease. The value of  $C_{33}^{\text{hcp}}$  remains nearly constant with changing Nb or Mo composition.

Using the above calculated  $C_{ij}$ , we assess the mechanical stability of each phase using the well-known Born

criteria [42,43]. In the case of cubic structures, elastic stability requires that

$$C_{11}^{\text{bcc}} - |C_{12}^{\text{bcc}}| > 0, \quad C_{11}^{\text{bcc}} + 2C_{12}^{\text{bcc}} > 0, \quad \text{and} \quad C_{44}^{\text{bcc}} > 0. \quad (1)$$

For the hexagonal structures, elastic stability requires that

$$C_{11}^{\text{hcp}} > |C_{12}^{\text{hcp}}|, \quad C_{33}^{\text{hcp}}(C_{11}^{\text{hcp}} + C_{12}^{\text{hcp}}) > 2(C_{13}^{\text{hcp}})^2, \\ \text{and } C_{44}^{\text{hcp}} > 0. \quad (2)$$

Compositions where the bcc structure or hcp structure is elastically unstable according the above criteria are highlighted in Fig. 5. In the bcc phase, alloys with low Nb or Mo content are unstable with respect to a tetragonal shear as  $C' = (C_{11}^{\text{bcc}} - C_{12}^{\text{bcc}})/2 < 0$ . Mechanical stability is predicted above  $x_{\text{bcc}}^C = 10$  at.% for Nb, and  $x_{\text{bcc}}^C = 4$  at.% for Mo. In the hcp phase, elastic stability is predicted for concentrations of Nb below 19 at.% in  $(\text{TiZrHf})_{1-x}\text{Nb}_x$  and concentrations of Mo below 10 at.% in  $(\text{TiZrHf})_{1-x}\text{Mo}_x$ . The alloys with Nb or Mo content above these thresholds are predicted to be elastically unstable due to violation of  $C_{66}^{\text{hcp}} = (C_{11}^{\text{hcp}} - C_{12}^{\text{hcp}})/2 < 0$ . Moreover, it is found that, at the same composition  $x$ ,  $C'$  of the bcc  $(\text{TiZrHf})_{1-x}\text{Mo}_x$  alloy is larger than that of bcc  $(\text{TiZrHf})_{1-x}\text{Nb}_x$ , and vice versa for  $C_{66}^{\text{hcp}}$ . These results demonstrate that the bcc elastic hardening and hcp softening effects of Mo are more pronounced than those of Nb. Furthermore, our obtained results imply that the relative effect of the alloying elements on the mechanical stability is mainly dominated by the  $d$ -band filling.

From the above phase stability and mechanical stability study, our results suggest that the addition of the group three transition metals, e.g., Nb, may offer a larger composition interval to develop TRIP  $(\text{TiZrHf})_{1-x}\text{TM}_x$  alloy compared to the addition of group four ones.

### E. Micromechanical properties

Based on the results of phase stability and mechanical stability studied above, we further investigate the mechanical properties of  $(\text{TiZrHf})_{1-x}\text{Nb}_x$  and  $(\text{TiZrHf})_{1-x}\text{Mo}_x$  alloys. We first compute the single-crystal Young's modulus  $Y_{[hkl]}$  in several high-symmetry directions and the anisotropy factors  $f_Y$  as defined in Ref. [44], which are listed in Table I:

$$f_Y^{\text{hcp}} = \frac{C_{33}^{\text{hcp}}C_{11}^{\text{hcp}} - (C_{13}^{\text{hcp}})^2}{(C_{11}^{\text{hcp}})^2 - (C_{12}^{\text{hcp}})^2} \\ \text{and } f_Y^{\text{bcc}} = \frac{2C_{44}^{\text{bcc}}(C_{11}^{\text{bcc}} + 2C_{12}^{\text{bcc}})}{C_{11}^{\text{bcc}}(C_{11}^{\text{bcc}} + C_{12}^{\text{bcc}}) - 2(C_{12}^{\text{bcc}})^2}. \quad (3)$$

The calculated directional dependence of single-crystal  $Y_{[hkl]}$  and  $f_Y$  for the selected alloys in the bcc and hcp phases are shown in Table I. In the bcc phase, one can see that the [100] and [111] directions have the lowest and highest single-crystal Young's modulus, respectively. The observed trend is that the single-crystal Young's modulus in the [100] and [110] directions increases as the concentration of Nb/Mo increases, whereas it slightly decreases in the [111] direction. In the hcp phase, the single-crystal Young's modulus in the [210] direction is sharply reduced by the addition of Nb and Mo, while it remains approximately constant in the [001] direction with Nb addition and slightly decreases with Mo.

Turning to the anisotropy factors  $f_Y$ , a larger deviation of it from one indicates a larger dependence of  $Y$  on the loading direction. One can see from Table I,  $f_Y^{\text{bcc}}$  of most

TABLE I. The calculated single-crystal Young's modulus in several high-symmetry directions (in units of GPa) and the calculated anisotropy factor,  $f_Y$ . Entries denoted by ... were omitted due to elastic instability.

RHEA	bcc phase				hcp phase		
	$Y_{[110]}$	$Y_{[100]}$	$Y_{[111]}$	$f_Y^{\text{bcc}}$	$Y_{[210]}$	$Y_{[001]}$	$f_Y^{\text{hcp}}$
TiZrHf	...	...	...	...	118.5	171.4	1.5
$(\text{TiZrHf})_{90}\text{Nb}_{10}$	32.0	9.4	159.9	19.6	69.6	173.4	2.5
$(\text{TiZrHf})_{87}\text{Nb}_{13}$	47.6	15.4	157.3	11.7	50.1	172.3	3.4
$(\text{TiZrHf})_{84}\text{Nb}_{16}$	62.9	22.5	157.2	7.9	27.7	171.3	6.2
$(\text{TiZrHf})_{81}\text{Nb}_{19}$	66.9	24.9	152.9	6.9	1.5	169.9	112.0
$(\text{TiZrHf})_{75}\text{Nb}_{25}$	86.9	38.6	148.7	4.2	...	...	...
$(\text{TiZrHf})_{84}\text{Nb}_{40}$	106.9	64.9	136.1	2.2	...	...	...
$(\text{TiZrHf})_{93}\text{Mo}_7$	43.0	13.5	157.9	13.4	45.3	163.6	3.6
$(\text{TiZrHf})_{91}\text{Mo}_9$	46.0	14.8	154.0	11.8	15.0	160.5	10.3
$(\text{TiZrHf})_{90}\text{Mo}_{10}$	50.8	16.8	156.3	10.6	...	...	...
$(\text{TiZrHf})_{81}\text{Mo}_{19}$	103.0	55.0	145.2	2.8	...	...	...
$(\text{TiZrHf})_{75}\text{Mo}_{25}$	107.5	63.5	139.9	2.3	...	...	...
$(\text{TiZrHf})_{60}\text{Mo}_{40}$	123.6	115.1	126.7	1.1	...	...	...

of the considered alloys are much larger than one, implying strong anisotropy in  $Y$ , and the addition of Nb introduces a larger effect on  $f_Y^{\text{bcc}}$  compared to that of Mo. We find that the value of  $f_Y$  is reduced with increasing Nb or Mo in the bcc phase, whereas it is enlarged in the hcp phase. In either phase, the anisotropy of  $f_Y$  is more pronounced the closer the alloy composition is to the point where the phase becomes mechanically unstable (Fig. 5).

Figure 6 presents the full directional dependence of  $Y_{[hkl]}$  for  $(\text{TiZrHf})_{90}\text{Nb}_{10}$  and  $(\text{TiZrHf})_{87}\text{Nb}_{13}$  alloys in the hcp and bcc phases. A clear correlation between the magnitude of the  $f_Y$  and the shape of the Young's modulus surface is apparent, i.e.,  $(\text{TiZrHf})_{90}\text{Nb}_{10}$  is more (less) anisotropic than  $(\text{TiZrHf})_{87}\text{Nb}_{13}$  in the bcc (hcp) phase. A similar situation is observed for the  $(\text{TiZrHf})_{1-x}\text{Mo}_x$  alloys (not shown). Using the Voigt-Reuss-Hill averaging method [45], we determine the polycrystalline Young's modulus  $Y$ , bulk modulus  $B$ , and shear modulus  $G$  from the calculated single-crystal elastic constants. For the hcp TiZrHf, our obtained  $Y$  is 123.7 GPa, which is in good agreement with the available experimental data  $116.51 \pm 2.82$  GPa [31]. Figure 7 displays the derived elastic moduli for the selected  $(\text{TiZrHf})_{1-x}\text{Nb}_x$  and  $(\text{TiZrHf})_{1-x}\text{Mo}_x$  alloys in their bcc and hcp phases. For both  $(\text{TiZrHf})_{1-x}\text{Nb}_x$  and  $(\text{TiZrHf})_{1-x}\text{Mo}_x$  alloy systems, one can see that all the moduli in the bcc phase increase with increasing Nb or Mo composition. Turning to the hcp phase, it can be seen that  $Y$  and  $G$  drop sharply, and  $B$  weakly increases with the addition of Nb or Mo. For example, the decrease in  $G$  and  $Y$  are about 74% and 71%, respectively, when 19 at.% Nb is added. For  $(\text{TiZrHf})_{1-x}\text{Nb}_x$ , we observe that the alloys with  $x \leq 13$  at.% have larger  $G$  and  $Y$  in the hcp phase than in the bcc phase, while the bcc phase has larger moduli above the critical content 13 at.%. For the  $(\text{TiZrHf})_{1-x}\text{Mo}_x$  alloys, its  $G$  and  $Y$  behave similarly to those of the  $(\text{TiZrHf})_{1-x}\text{Nb}_x$  alloy and the critical concentration  $x$  is about 7 at.%. For all considered alloys, the bulk modulus  $B$  in the hcp phase is slightly larger than that in the bcc phase. Overall, the

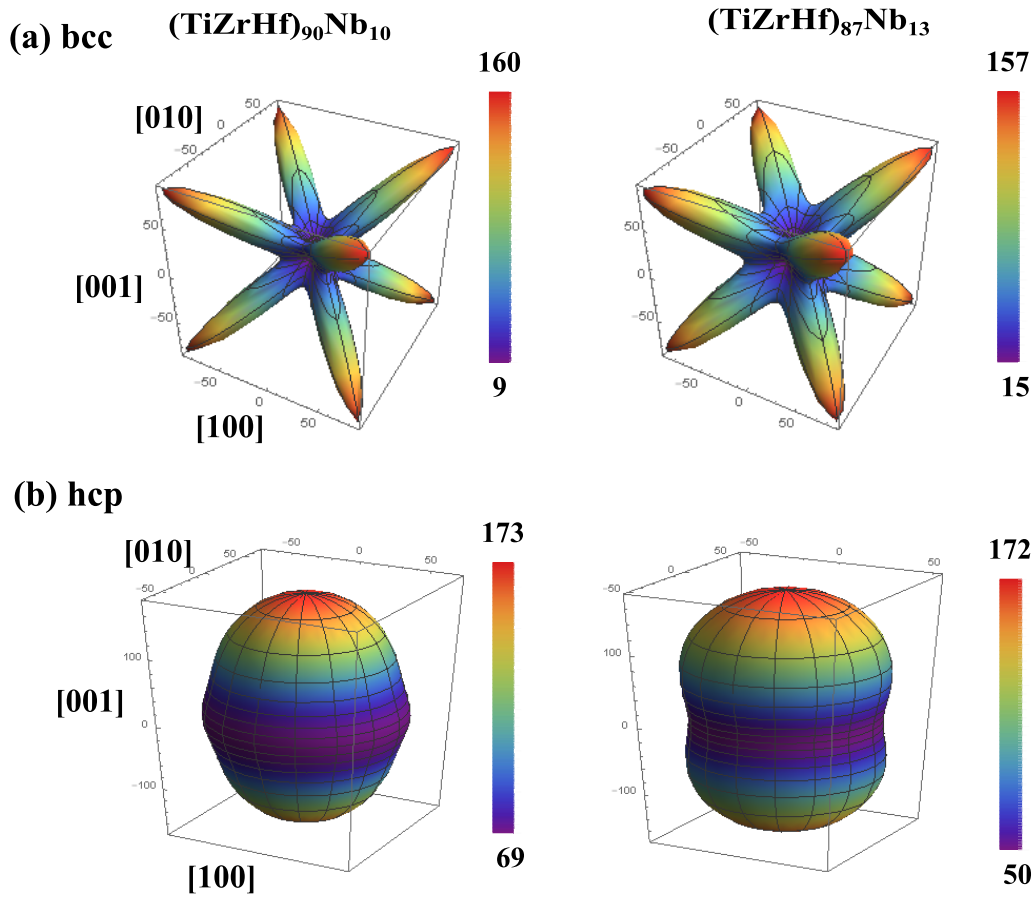


FIG. 6. The full directional dependence of single-crystal Young’s modulus  $Y_{[hkl]}$  (in units of GPa) for the  $(\text{TiZrHf})\text{Nb}_{10}$  and  $(\text{TiZrHf})\text{Nb}_{13}$  alloys in the bcc and hcp phases.

influence of Mo on the moduli in both bcc and hcp phases is more significant than that of Nb, e.g., the polycrystalline elastic moduli  $Y$  and  $G$  in the hcp phase decrease faster with increasing Mo concentration than with the Nb addition. At these particular Nb and Mo contents ( $\approx 13$  at.% and 7 at.%,

respectively),  $B$ ,  $G$ , and  $Y$  of the hcp phase are nearly identical to the respective moduli of the bcc phase. There are two reasons for this. First, there are only two independent elastic moduli in homogeneous isotropic linear elastic materials, e.g.,  $B$  and  $Y$ . Second,  $B^{\text{hcp}}$  and  $B^{\text{bcc}}$  have similarly magnitude and alloying

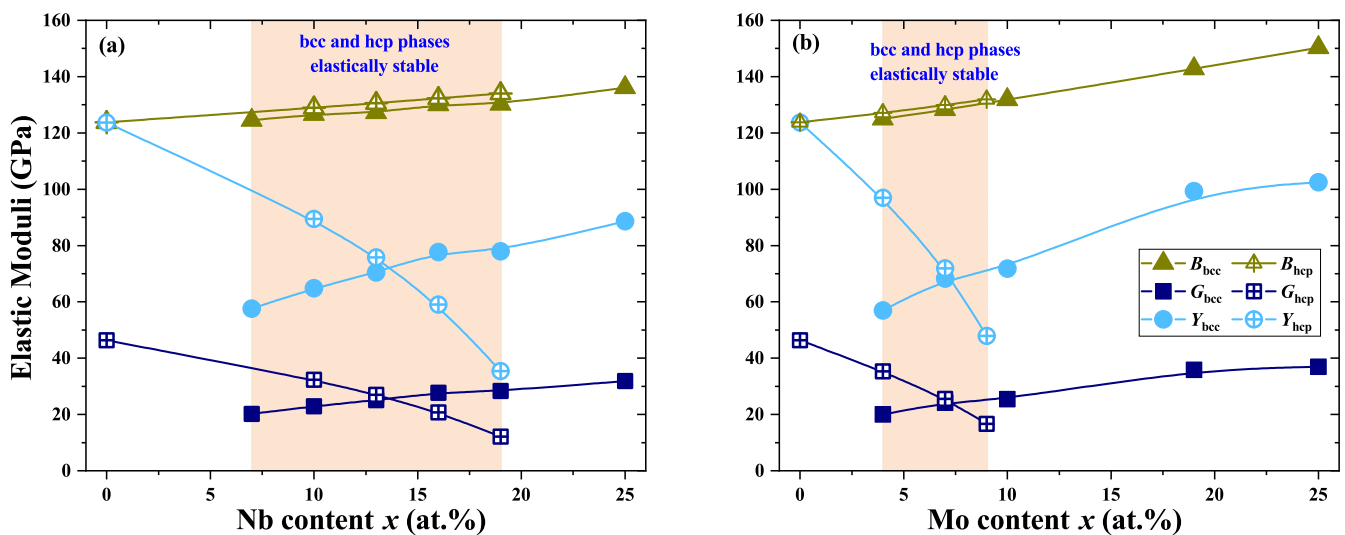


FIG. 7. The calculated composition dependence of polycrystalline elastic moduli for the  $(\text{TiZrHf})_{1-x}\text{Nb}_x$  and  $(\text{TiZrHf})_{1-x}\text{Mo}_x$  alloys in the bcc and hcp phases. Composition intervals where both the bcc and hcp phases are mechanically stable are highlighted.

trends, while  $Y^{\text{hcp}}$  and  $Y^{\text{bcc}}$  have opposite alloying trends (see Fig. 7).

Considering that newly formed hcp phase during deformation may share the load at late deformation stage [18], the hcp phase may be preferred to have a higher Young's modulus than the bcc phase. According to our predicted composition dependence polycrystalline Young's modulus  $Y$  in the bcc and hcp phases (Fig. 7), the content of the TM alloying elements has to be carefully chosen to develop desired properties.

#### IV. CONCLUSION

In summary, a first-principles investigation of the crystal lattice parameters, the phase stability, and the micromechanical properties of the  $(\text{TiZrHf})_{1-x}\text{TM}_x$  (TM=V, Nb, Cr, Mo, and W) alloys was presented. It was found that the addition of the TM elements leads to a decrease in the Wigner-Seitz radius  $w$  in both the bcc and hcp phases and an increase in the hexagonal  $c/a$  ratios. In both the bcc and hcp phases, the reduction of the  $w$  is the strongest with adding Cr and the weakest with Nb. The calculated  $\Delta E^{\text{bcc-hcp}}$  indicated that the relative stability between compositionally equivalent bcc and hcp phases can be tuned and inverted. The results suggested that Mo and W are stronger bcc stabilizers compared to V and Nb, while Cr has an intermediate effect, indicating that the addition of V or Nb offers the largest composition interval where the bcc phase is metastable. Our calculated results for the  $(\text{TiZrHf})_{1-x}\text{Nb}_x$  and  $(\text{TiZrHf})_{1-x}\text{Mo}_x$  alloys suggested that the bcc phase is mechanically stable above the

critical concentration  $x = 10$  at.% for Nb, and  $x = 4$  at.% for Mo. The critical concentration above which the hcp phase becomes the unstable phase was found to be around 19 at.% and 10 at.% for  $(\text{TiZrHf})_{1-x}\text{Nb}_x$  and  $(\text{TiZrHf})_{1-x}\text{Mo}_x$ , respectively. The calculated elastic constants demonstrated that the bcc elastic hardening and the hcp softening effects of Mo are more pronounced than those of Nb. The obtained  $f_Y$  indicated that the bcc phase is more elastically anisotropic than the hcp phase. For both the  $(\text{TiZrHf})_{1-x}\text{Nb}_x$  and  $(\text{TiZrHf})_{1-x}\text{Mo}_x$  alloy systems, all the derived polycrystalline moduli in the bcc phase increased with increasing Nb or Mo composition, whereas the Young's and shear moduli were starkly reduced in the hcp phase. Our results revealed that the hcp phase has higher shear and Young's moduli than the bcc phase below a critical composition for the Nb or Mo addition, while the bcc phase has larger moduli above the critical composition. Furthermore, we found that the phase stability and the mechanical properties are mainly determined by the  $d$ -band filling.

#### ACKNOWLEDGMENTS

The Swedish Research Council, the Göran Gustafssons Foundation, the Carl Tryggers Foundation, and the Swedish Foundation for Strategic Research are acknowledged for financial support. The computations were enabled by resources provided by the National Academic Infrastructure for Supercomputing in Sweden (NAISS) at Linköping, partially funded by the Swedish Research Council through Grant Agreement No. 2022-06725.

- 
- [1] O. N. Senkov, G. B. Wilks, D. B. Miracle, C. P. Chuang, and P. K. Liaw, *Intermetallics* **18**, 1758 (2010).
- [2] S. Maiti and W. Steurer, *Acta Mater.* **106**, 87 (2016).
- [3] Y. D. Wu, Y. H. Cai, T. Wang, J. J. Si, J. Zhu, Y. D. Wang, and X. D. Hui, *Mater. Lett.* **130**, 277 (2014).
- [4] O. Senkov, G. B. Wilks, J. M. Scott, and D. B. Miracle, *Intermetallics* **19**, 698 (2011).
- [5] F. Maresca and W. A. Curtin, *Acta Mater.* **182**, 235 (2020).
- [6] T. Nagase, S. Anada, P. D. Rack, J. H. Noh, H. Yasuda, H. Mori, and T. Egami, *Intermetallics* **38**, 70 (2013).
- [7] O. A. Waseem, J. Lee, H. M. Lee, and H. J. Ryu, *Mater. Chem. Phys.* **210**, 87 (2018).
- [8] O. A. Waseem and H. J. Ryu, *Sci. Rep.* **7**, 1926 (2017).
- [9] Y. Iijima, T. Nagase, A. Matsugaki, P. Wang, K. Ameyama, and T. Nakano, *Mater. Des.* **202**, 109548 (2021).
- [10] A. Motallebzadeh, N. Peighambaroust, S. Sheikh, H. Murakami, S. Guo, and D. Canadinc, *Intermetallics* **113**, 106572 (2019).
- [11] Y. Yuan, Y. Wu, Z. Yang, X. Liang, Z. Lei, H. Huang, H. Wang, X. Liu, K. An, W. Wu, and Z. Lu, *Mater. Res. Lett.* **7**, 225 (2019).
- [12] R. Thomson, *Solid State Phys.* **39**, 1 (1986).
- [13] E. Mak, B. Yin, and W. Curtin, *J. Mech. Phys. Solids* **152**, 104389 (2021).
- [14] X. Li, W. Li, D. L. Irving, L. K. Varga, L. Vitos, and S. Schönecker, *Acta Mater.* **189**, 174 (2020).
- [15] Z. Lei, X. Liu, Y. Wu, H. Wang, S. Jiang, S. Wang, X. Hui, Y. Wu, B. Gault, P. Kontis, D. Raabe, L. Gu, Q. Zhang, H. Chen, H. Wang, J. Liu, K. An, Q. Zeng, T. Nieh, and Z. Lu, *Nature (London)* **563**, 546 (2018).
- [16] Z. An, S. Mao, T. Yang, C. Liu, B. Zhang, E. Ma, H. Zhou, Z. Zhang, L. Wang, and X. Han, *Mater. Horiz.* **8**, 948 (2021).
- [17] L. Liliensten, J.-P. Couzinié, J. Bourgon, L. Perrière, F. P. G. Dirras, and I. Guillot, *Mater. Res. Lett.* **5**, 110 (2017).
- [18] H. Huang, Y. Wu, J. He, H. Wang, X. Liu, K. An, W. Wu, and Z. Lu, *Adv. Mater.* **29**, 1701678 (2017).
- [19] S. Wang, S. Lu, M. Wu, D. Wang, G. Zhu, C. Yang, D. Shu, B. Sun, and L. Vitos, *Mater. Sci. Eng. A* **832**, 142476 (2022).
- [20] D. Wei, X. Li, J. Jiang, W. Heng, Y. Koizumi, W. M. Choi, B. J. Lee, H. S. Kim, H. Kato, and A. Chiba, *Scr. Mater.* **165**, 39 (2019).
- [21] Z. Li, F. Körmann, B. Grabowski, J. Neugebauer, and D. Raabe, *Acta Mater.* **136**, 262 (2017).
- [22] R. Feng, G. Kim, D. Yu, Y. Chen, W. Chen, P. K. Liaw, and K. An, *Mater. Des.* **219**, 110820 (2022).
- [23] X. Li, *Acta Mater.* **142**, 29 (2018).
- [24] O. K. Andersen, O. Jepsen, and G. Krier, in *Lectures on Methods of Electronic Structure Calculations*, edited by V. Kumar, O. K. Andersen, and A. Mookerjee (World Scientific, Singapore, 1994), p. 63.
- [25] L. Vitos, *Phys. Rev. B* **64**, 014107 (2001).
- [26] P. Hohenberg and W. Kohn, *Phys. Rev.* **136**, B864 (1964).
- [27] J. P. Perdew and Y. Wang, *Phys. Rev. B* **45**, 13244 (1992).

- [28] B. L. Gyorffy, *Phys. Rev. B* **5**, 2382 (1972).
- [29] L. Vitos, *Computational Quantum Mechanics for Materials Engineers* (Springer-Verlag, London, 2007).
- [30] X. Li, H. Zhang, S. Lu, W. Li, J. Zhao, B. Johansson, and L. Vitos, *Phys. Rev. B* **86**, 014105 (2012).
- [31] B. Akhil, A. B. Bajpai, and K. Biswas, *Philos. Mag. Lett.* **102**, 287 (2022).
- [32] P. Singh, S. Gupta, S. Thimmaiah, B. Thoeny, P. K. Ray, A. V. Smirnov, D. D. Johnson, and M. J. Kramer, *Acta Mater.* **194**, 540 (2020).
- [33] S. Cotes, A. Baruj, M. Sade, and A. F. Guillermet, *J. Physique III* **5**, C2-83 (1995).
- [34] S. Cotes, A. Guillermet, and M. Sade, *Mater. Sci. Eng. A* **273-275**, 503 (1999).
- [35] S. Wang, D. Wu, H. She, M. Wu, D. Shu, A. Dong, H. Lai, and B. Sun, *Mater. Sci. Eng. C* **113**, 110959 (2020).
- [36] V. L. Moruzzi, A. R. Williams, and J. F. Janak, *Phys. Rev. B* **15**, 2854 (1977).
- [37] H. L. Skriver, *Phys. Rev. B* **31**, 1909 (1985).
- [38] J. X. Zheng-Johansson, O. Eriksson, and B. Johansson, *Phys. Rev. B* **59**, 6131 (1999).
- [39] D. G. Pettifor, *Bonding and Structure of Molecules and Solids* (Oxford University Press, Oxford, 1995).
- [40] J. B. Staunton, S. S. A. Razee, M. F. Ling, D. D. Johnson, and F. J. Pinski, *J. Phys. D: Appl. Phys.* **31**, 2355 (1998).
- [41] M. Sigalas, D. A. Papaconstantopoulos, and N. C. Bacalis, *Phys. Rev. B* **45**, 5777 (1992).
- [42] M. Born, *Proc. Cambridge Philos. Soc.* **36**, 160 (1940).
- [43] M. Born and K. Huang, *Dynamical Theory of Crystal Lattices* (Oxford University Press, London, 1954).
- [44] D. Tromans, *Int. J. Res. Rev. Appl. Sci.* **6**, 462 (2011).
- [45] R. Hill, *Proc. Phy. Soc. A* **65**, 349 (1952).